JOURNAL OF MATERIALS SCIENCE 32 (1997) 2451–2467

Characterization of severe matrix distortions during phase separation from the redistribution of diffracted intensities

R. KUŽEL
Department of Semi-Conductor Physics, Charles University, Praha 2, Czechoslovakia

B. HE, C. R. HOUSKA
Department of Materials Science and Engineering, Virginia Polytechnic Institute and State University, Blacksburg, VA 24061, USA

Severe matrix deformation has been examined at an early stage of age-hardening in a polycrystalline Brush 25 alloy containing Cu–11.50 at % Be–0.23 at % Co aged at 200 °C. Simplified anisotropic elastic models for the atomic displacement field about coherent disc-shaped precipitates provide quantitative estimates of the atomic displacement field in the surrounding matrix. This requires a separation of diffracted intensity into Bragg peaks, static diffuse scattering, and quasilines. The latter originates from the severely distorted zone about the precipitates. Elastic models include single discs, and [1 0 1] stair-step pairs. Ageing at 200 °C introduces larger changes in the diffraction profiles than at 315 °C. This is observed mainly as large variations in quasiline intensities, as well as in their relative peak positions. Comparisons are made at about one-half the maximum hardness. These variations result from the response of the coherent anisotropic copper matrix to large tetragonal Bain strains in disc-shaped precipitates, and a strong preference for the largest deformations to be perpendicular to the free surface. Quasiline shifts are used along with Végard's Law to extend the metastable Guinier–Preston (GP)-zone boundary to 200 °C. This boundary extension is smooth and continuous with published data, and thereby relates the metastable GP boundary to a highly distorted matrix about disc-shaped precipitates. Disc diameters range from 4.8–6.4 nm with a thickness of 0.29 nm after 16–64 h at 200 °C. The [1 0 1] stair-step pair model best fits the experimental results.

1. Introduction

Certain age-hardenable alloy systems can produce zones of large matrix deformations about precipitates having a size misfit with the surrounding matrix. These zones grow with ageing and give special diffraction effects. This includes a partitioning of the sharp Bragg peaks into somewhat broader static diffuse scattering, and quasilines [1]. Our theoretical and experimental efforts have been directed towards a quantitative investigation of this behaviour in a polycrystalline Cu–Be–Co alloy. Ageing at low temperatures, for times shorter than a time giving maximum hardness, gives this interesting mix of three types of scattering that all become quasilines before maximum hardness is attained.

A detailed model describing this phenomenon requires time-consuming calculations that have been carried out only at selected ageing times [2]. These are capable of fitting X-ray diffraction (XRD) profile shapes resulting from structural changes taking place in the matrix and the precipitate of aged alloys. In this paper, a simplified procedure is described in terms of a precipitate model that gives agreement with the XRD integrated intensities as well as other general trends in the scattering.

Theory has been developed [1] which is based upon concepts originally proposed by Krivoglaz [3]. However, the interplay with quantitative XRD data provides new insights and plays an important role in the overall analysis and the interpretation of the data. This has required the development of models for the displacement field from precipitates which includes an anisotropic displacement field from combinations of disc-shaped precipitates [4]. These displacement fields serve as input for the calculation of the exponential attenuation factor, $2M$, which determines the partitioning of matrix scattering into its three parts. An experimental approach is described for determining $2M$ by unscrambling the data for matrix scattering into its three components [1]. The relative integrated intensities for each matrix peak, having a range of widths, is given by

$$\text{Bragg (B)} \quad e^{-2M} \tag{1}$$

$$\text{Static diffuse (SD)} \quad 2Me^{-2M} \tag{2}$$

$$\text{Quasiline (Q)} \quad 1 - e^{-2M} - 2Me^{-2M} \tag{3}$$

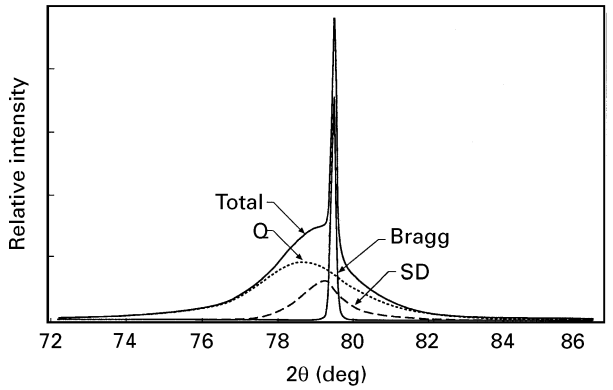

Figure 1 (2 0 0) powder diffraction peak resulting from a −20% strain acting perpendicular to a thin ellipsoid zone in a copper matrix with semi-axis $a = b = 3.5$ and $c = 0.7$ nm. Cr$K_{\alpha 1}$ radiation was used to calculate the 2θ scale. For these conditions, $2M = 2.4$.

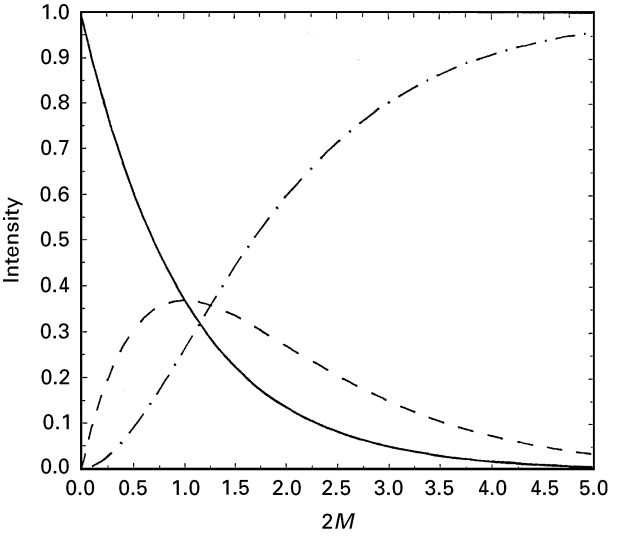

Figure 2 Partitioning of integrated intensites versus $2M$ into (——) Bragg, (– – –) static diffuse (SD), and (—·—) quasiline (Q).

The second and third components represent diffuse scattering that has sharpened into Bragg-like peaks. For coherent precipitation, the Bragg peaks normally remain unshifted at the 2θ position found in the as-quenched solid solution. The *SD* peaks are very close to or at the Bragg peak as mainly Huang diffuse scattering; however, a tail portion may extend some distance from the Bragg peaks. Quasilines can display the largest shift from the Bragg positions by varying amounts, but this typically is not large. Our present experience with a Cu–Be–Co alloy indicates that the shift requires an elastic displacement field that is anisotropic, making it noticeably dependent upon the permutation of the indices of the diffracting planes. Quasilines are broader by a factor of two to three than the SD component, with the SD having an intermediate apparent width when compared with the sharp Bragg peak. This may be seen in Fig. 1 showing powder diffraction simulations of a possible (2 0 0) peak for a Cu–Be alloy. The quasiline, static diffuse, and Bragg scattering are illustrated separately and as combined total scattering for $2M = 2.4$.

Fig. 2 illustrates partitioning of the three components with increasing $2M$, which increases with the severity of the displacement field and with peaks located at larger distances in reciprocal space. At small $2M$, which is found for as-quenched systems, only Bragg and a very broad SD are important. For $2M \sim 1$, all three are equally important, while for $2M > 5$, the Bragg peak is seen to vanish. Our procedure examines samples within the range $0.5 < 2M < 5$. Although the Bragg peak contributes only $\sim 5\%$ of the intensity, its sharpness allows it to be barely perceptible at $2M \sim 5$.

This behaviour can be understood qualitatively from Fig. 3a. Consider a crystal having N_3 cells along columns oriented perpendicular to the diffracting planes ($h\,k\,l$). The sources of lattice distortion originate at precipitates depicted by heavy dots. The dimension of the zone of severe distortion is given by n_Q, while the limit of weak elastic coupling is given by n_B for pairs of cells within a column oriented perpendicular to planes with indices ($h\,k\,l$). Beyond the distance, n_B, pairs of cells are no longer coupled, because the displacement field at large distances decreases inversely as the square of the distance. Instead, the displacement of pairs of cells beyond n_B become independent and are determined by precipitates located in the proximity of each cell in the pair. The detailed shape of the intensity diffracted from such a column is representable by a Fourier series containing coefficients with projected column displacements perpendicular to the ($h\,k\,l$) planes. This can be conveniently separated into

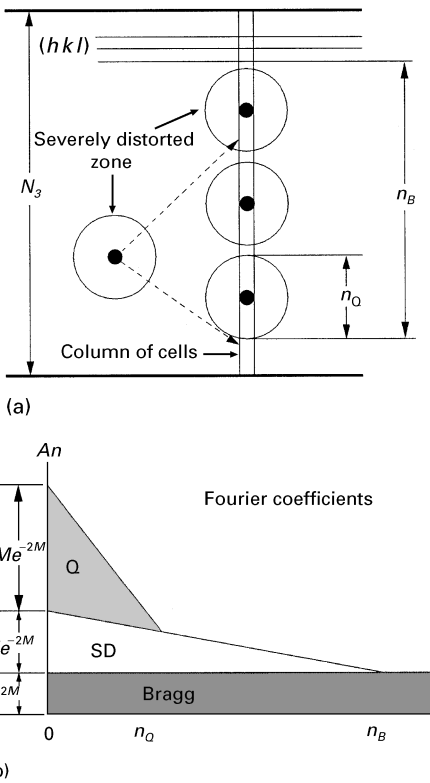

Figure 3 (a) Schematic representation of crystal, illustrating severely distorted zones with displacement centres acting on a column. n_Q and n_B provide approximate dimensions of the severely distorted zones and range of coupling for pairs of cells within a column. (b) Schematic representation of Fourier coefficients showing approximate cutoff points, n_Q and n_B, which influence the sharpness of Fourier series describing quasilines and static diffuse.

three parts. The Fourier series describing the quasiline contains Fourier coefficients whose number is determined by an upper limit, n_Q, which may be estimated from the diameter of the precipitate over the $2M$ range under consideration. The dimensioning of the Fourier series describing the *SD* is determined by the limit, n_B.

With increasing size of a coherent precipitate and a decreasing density, the size of the severely distorted zone, n_Q, increases. Consequently, the quasiline sharpens because its Fourier series representation contains Fourier coefficients that converge more slowly to a larger limiting value of n_Q (see Fig. 3b). This further increases the fractional contribution of quasiline, because $2M$ must increase with the strength of the field. An increasing precipitate size and strength increases n_B. A similar argument applies to the convergence and dimensioning of the Fourier series describing the SD, with an associated sharpening and a fractional contribution that at first increases and then decreases. The latter occurs when the overall matrix becomes dominated by the severely distorted zone. Also, as the lattice distortion becomes more severe, a smaller fraction of cells along columns remain uncoupled. This reduced volume fraction of uncoupled cells results in an overall attenuation of the sharp Bragg peak. However, if N_3 is large, there are a sufficient number of terms in the Fourier representation of the Bragg peak to maintain its sharpness. Clearly a full integration over all three components gives the classical integrated intensity expression [1]. The preceding discussion should be limited to approximately $2M < 5$. With an even more severe matrix fields and larger severely distorted zones that impinge upon each other, the quasilines could begin to broaden.

2. Calculation of $2M$

2.1. Point source

For precipitation problems, $2M$ may be calculated as a sum over column displacements $Z_{m_3 t}\, d_0$ [1, 3]

$$M = X_c \sum_t [1 - \cos(2\pi l_0 Z_{m_3 t})] \tag{4a}$$

where m_3 is the column location or and an equivalent volume integral with

$$M = \frac{X_c}{V_a} \int_{V_c}^{\infty} \{1 - \cos [k_0\, Z_{m_3}\, d_0]\}\, \mathrm{d}V \tag{4b}$$

where V_a is the atomic volume, X_c represents the fraction of sites occupied by the centre of a precipitate, and $k_0 = 2\pi\ l_0/d_0 = 4\pi \sin\theta/\lambda$. The order integers l_0 and d_0 are obtained from the interplanar spacing

$$d = \frac{a}{(h^2 + k^2 + l^2)^{1/2}} = \frac{d_0}{l_0} \quad \text{with } l_0 = 1, 2, \ldots \tag{5}$$

for a cubic matrix. Here the lowest order d-spacing ($l_0 = 1$) gives d_0 in terms of the lattice parameter, a, of the cubic cell and cubic Miller indices. The direction of d_0 lies along columns perpendicular to the $(h\,k\,l)$ planes. If an inverse-square dependence is assumed and the strength term, $A(\phi, \alpha)$ is anisotropic, the projected displacement is

$$Z_{m_3} d_0 = \frac{A(\phi, \alpha)}{r^2} \cos\chi \tag{6}$$

where r is the radial distance in reciprocal space, χ is the projection angle, and ϕ and α are angles which enter into its calculation. Because the scattered intensity is localized near each $(h\,k\,l)$ point in reciprocal space, the displacements entering the intensity expression may be taken as projected parallel to the diffraction vector, H_{hkl}. This allows attention to be focused on displacements along columns arranged perpendicular to the reflecting planes of the matrix. Therefore, $Z_{m_3} d_o$, might be considered as one of many projections onto H_{hkl} for a cell located in column m_1, m_2 at a column location m_3. This is located by the vector $\boldsymbol{r}$ with an origin at the centre of a precipitate. Fig. 4a and b illustrate and define the angles entering into the calculation of the projection angle, χ, as well as those entering into the calculation of the displacement field, i.e. ϕ and α.

Equation 4a was developed assuming that precipitates are randomly positioned on one habit plane. Additional crystallographically equivalent orientations of ellipsoidal or disc-shaped precipitates may be required to maintain the required crystal symmetry.

Equation 4b is readily integrated, with $\mathrm{d}V = -r^2\, \mathrm{d}x\, \mathrm{d}\alpha\, \mathrm{d}r$ and $x = \cos\phi$, changing variables for the radial integration

$$y = \frac{[k_0 A(\phi, \alpha) x]^{1/2}}{r} \tag{7}$$

and combining terms provides

$$M = \frac{X_c}{V_a} \int_0^{2\pi} \int_{-1}^{1} \int_0^{y_c} \times [k_0 A(\phi, \alpha) x]^{3/2}\, \frac{1 - \cos y^2}{y^4}\, \mathrm{d}y\, \mathrm{d}x\, \mathrm{d}\alpha \tag{8a}$$

with

$$y_c = \frac{[k_0 A(\phi, \alpha) x]^{1/2}}{r_c(\phi, \alpha)} \tag{8b}$$

In this case, we define

$$r_k = [k_0 A(\phi, \alpha) x]^{1/2} \tag{8c}$$

which is anisotropic and contains a projection term, x. The location of the precipitate–matrix interface is given by $r_c(\phi, \alpha)$. Consider only the integral over radial distance which can be carried out with a two-step integration by parts

$$\int_0^{y_c} \frac{(1 - \cos y^2)}{y^4}\, \mathrm{d}y = \frac{4}{3} \int_0^{y_c} \cos y^2\, \mathrm{d}y - \frac{2}{3^3_{y_c}} \left(y_c^2 \sin y_c^2 + \sin^2 \frac{y_c^2}{2} \right) \tag{9}$$

in the limit of $y_c = r_k/r_c \to \infty$, the zone of severe distortion becomes much larger than the precipitate for all directions and Equation 8a simplifies to

$$M(h\,k\,l) = \frac{X_c}{V_a} \frac{(2\pi)^{1/2}}{3} \int_0^{2\pi} \int_{-1}^{1} \times [k_0 A(\phi, \alpha) x]^{3/2}\, \mathrm{d}x \mathrm{d}\alpha \tag{10}$$

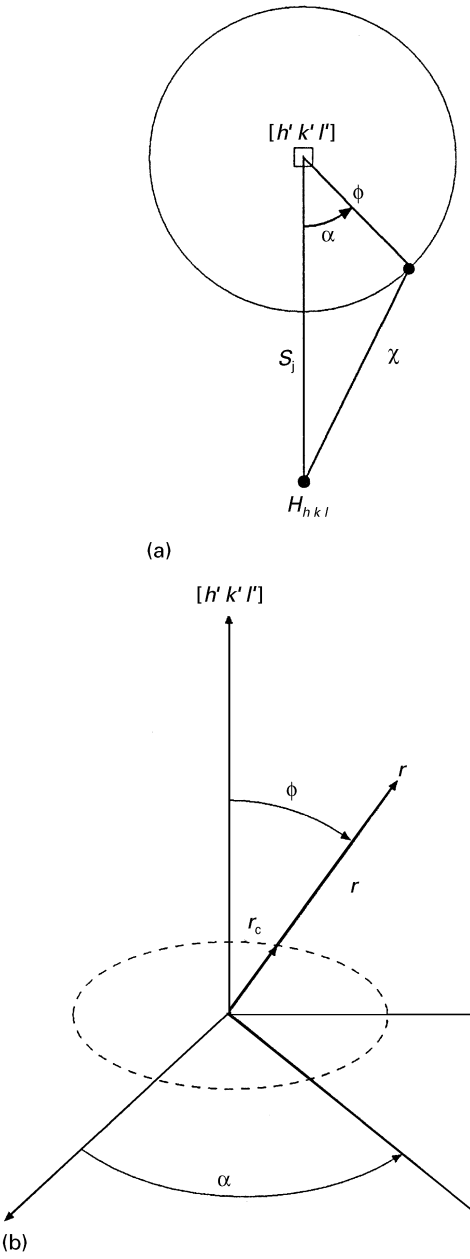

Figure 4 (a) The various angles as a spherical triangle entering into the projection with χ being the angle between the radial displacement along r and a column direction H_{hkl}, S_j the angle between the symmetry axis of a defect $[h'k'l']$ and H_{hkl}, and ϕ the angle between $[h'k'l']$ and the radial direction r. (b) The angles ϕ, α entering into the displacement field with r originating from the centre of the defect. r_c locates the precipitate surface.

M is determined by averaging over projected displacements originating from all orientations of $\boldsymbol{r}$

$$\langle [k_0 A(\phi, \alpha)x]^{3/2} \rangle = \frac{\int_0^{2\pi} \int_{-1}^{1} [k_0 A(\phi, \alpha)x]^{3/2} \, dx \, d\alpha}{\int_0^{2\pi} \int_{-1}^{1} dx \, d\alpha} \tag{11}$$

or

$$M(h\,k\,l) = \frac{4\pi(2\pi)^{1/2}}{3} \frac{X_c}{V_a} \langle [k_0 A(\phi, \alpha)x]^{3/2} \rangle \tag{12}$$

This gives a $(\sin\theta/\lambda)^{3/2}$ dependence of $2M$.

Weak fields correspond to the other extreme or small y_c. In other words, the radius r_k becomes much smaller than the precipitate r_c for all directions, and

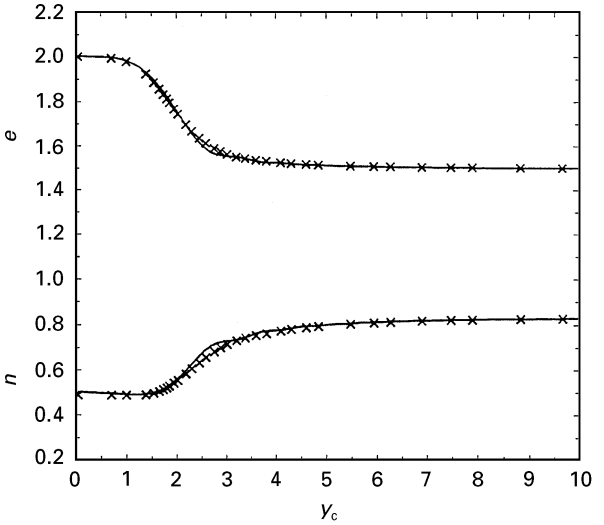

Figure 5 Dependence of exponential term, n, and coefficient e with y_c. (×) Numerical fitting, (—) analytical equation.

one obtains

$$M(h\,k\,l) = \frac{X_c}{V_a} \frac{1}{2} \int_0^{2\pi} \int_{-1}^{1} \frac{[k_0 A(\phi, \alpha)x]^2}{r_c(\phi, \alpha)} \, dx d\alpha \tag{13}$$

or, in terms of an average radial term taken over all angles ϕ and α

$$M(h\,k\,l) = \frac{2\pi X_c}{V_a} \frac{[k_0 A(\phi, \alpha)x]^2}{r_c(\phi, \alpha)} \tag{14}$$

The following form summarizes these limits giving extremes in n and the power of k_0

$$M(h\,k\,l) = 4\pi \frac{X_c}{V_a} e \left\langle \frac{[A(\phi, \alpha)x]^n}{r_c^{2n-3}(\phi, \alpha)} \right\rangle k_0^n \tag{15a}$$

$$n = \begin{cases} 2, & y_c \to 0 \quad \text{weak distortion} \\ \frac{3}{2}, & y_c \to \infty \quad \text{severe distortion} \end{cases} \tag{15b}$$

$$e = \begin{cases} \frac{1}{2}, & y_c \to 0 \quad \text{weak distortion} \\ \frac{2}{3}(\frac{\pi}{2})^{1/2} \approx 0.84, & y_c \to \infty \quad \text{severe distortion} \end{cases} \tag{15c}$$

The transitions for n and e are illustrated in Fig. 5 which was obtained by expansion about a central point of the data set (k_{00}). It is found that n and e can be taken as 2 and 1/2 for $0 \leqslant y_c \leqslant 1$. This requires that the radius of the severely distorted zone be smaller than the dimensions of the precipitate in each direction ϕ, α. Over this range in y_c, one finds that M varies as the square of the radial distance in reciprocal space. The square dependence is also found for the thermal attenuation factor M_T. If $y_c \geqslant 5$ the size of the severely distorted zone dominates $n \approx 3/2$ and $e \approx 0.8$. Our present interest is confined to the transition range $1 \leqslant y_c \leqslant 3$ in which the severely distorted zone grows beyond the precipitate dimension but does not extend over all of the matrix. Although both n and e are weak functions of y_c, they are included in Equation 15 and show the greatest variation in the more complicated transition region ($1 \leqslant y_c \leqslant 3$).

If the strength term $A(\phi, \alpha)$ and $r_c(\phi, \alpha)$ are isotropic, the average indicated in Equation 15a can be

carried out explicitly giving

$$M(h\,k\,l) = 4\pi e' \frac{X_c}{V_a} \frac{[k_0 A]^n}{r_c^{2n-3}} \tag{16a}$$

At two extreme cases

$$e' = \begin{cases} \frac{1}{6}, & y_c \to 0 \\ \frac{4}{15}\left(\frac{\pi}{2}\right)^{1/2} & y_c \to \infty \end{cases} \tag{16b}$$

and

$$e = e'(n+1)$$

with n behaving as in Equation 15b. Again, Fig. 5 illustrates the overall dependence on y_c. Equation 15a provides a simple result giving the dependence of specimen parameters such as the concentration of precipitates, X_c/V_a, the strength of the lattice disturbance due to individual precipitates, A, and precipitate radius, r_c. The same arguments relating y_c to n and e' (or e) hold if

$$y_c = \frac{(k_0 A)^{1/2}}{r_c}$$

with the Krivoglaz radius,

$$r_k = (k_0 A)^{1/2} \tag{17}$$

Equations 15a and 16a represent simplified forms not yet appearing in the literature that describe the more interesting transition with $1 \leqslant y_c \leqslant 3$. The extreme limiting cases for an isotropic field have been reported by Krivoglaz [3] and are in complete agreement with these results.

In order to calculate $M(h\,k\,l)$, a model is required for the elastic displacements. In the early stage of precipitation, we consider thin discs subjected to an apparent tetragonal transformation strain. A simple displacement field is already available for a precipitate in the form of a disc within an anisotropic matrix of copper [4]. It is based upon a tetragonal strain without moment and represents an asymptotic solution of the form

$$\mu(r, \phi, C_{sd}, C_e) = \frac{\boldsymbol{A}(\phi, C_{sd}, C_e)}{r^2}, \tag{18a}$$

with a vector strength given by

$$\boldsymbol{A}(\phi, C_{sd}, C_e) = \frac{\Delta V}{4\pi\gamma} \left\{ \frac{i_r}{2} (C_{sd} E_1 [3(1 - f(C_e)\cos^2\phi - 8.08\, f(C_e)\cos 4\phi \cos^2\phi - 1] + 2) - i_\phi\, 3C_{sd} \sin\phi\cos\phi \right\} \tag{18b}$$

The various quantities are defined as follows

$$E_1 = \frac{5\mu + 3\lambda}{\mu}, \tag{19a}$$

$$C_e = 1 - \frac{C_{11} - C_{12}}{2C_{44}}, \tag{19b}$$

$$\gamma = 3\,\frac{\lambda + 2\mu}{3\lambda + 2\mu} \tag{19c}$$

$$f(C_e) = 0.15 \text{ erf } C_e \tag{19d}$$

with Lame elastic constants

$$\lambda = \frac{1}{5}(C_{11} + 4C_{12} - 2C_{44}) \tag{20a}$$

$$\mu = \frac{1}{5}(C_{11} - C_{12} + 3C_{44}) \tag{20b}$$

written in terms of the elastic constants. i_r and i_ϕ are unit vectors along the radial and tangential directions. The volume change for each disc-shaped precipitate is

$$\Delta V = \pi X_d V_{SF} S r_0^3 \tag{21a}$$

$$S = \frac{h}{r_0} \tag{21b}$$

where, X_d is the fraction of undersized or oversized atoms in the precipitate, V_{SF} is the volume size factor or the fractional change in atomic volume with respect to the atomic fraction of B, x_B (see King [5]). r_0 and h are the radius and height of the disc, E_1 is an elastic constant defined in terms of Lame's constants. C_s and C_d are the separate strengths of the spherical and doublet components of the displacement fields which may be expressed in terms of a single parameter C_{sd} [4], i.e.

$$C_s = (1 - C_{sd})\,\frac{V_{SF} V_a}{4\pi\gamma} \tag{22a}$$

$$C_d = 3C_{sd}\,\frac{V_{SF} V_a}{4\pi\gamma} \tag{22b}$$

with

$$C_{sd} = \frac{C_d}{3C_s + C_d} = \frac{P_{33} - P_{11}}{2P_{11} + P_{33}} \tag{23a}$$

with P_{33} and P_{11} representing the components of the dipole tensor that are associated with a tetragonal field. Integrating Equation 18a over a spherical surface surrounding the point defect, gives a volume change $V_{SF}\,V_a/\gamma$ per defect in an infinite medium. V_a has been tabulated by King [5]. Anisotropy has been introduced empirically through $f(C_e)$ and an anistropy factor defined by C_e with single-crystal elastic constants C_{11}, C_{44}, and C_{12}.

Equation 18a can be reduced to the Keating–Goland (K–G) expression for a loop [6] in an isotropic medium by setting $C_e = 0$, $x_d\,V_{SF}\,S r_0^3 = b r_0^2$, and $C_{sd} = (1 - 2\nu)/(1 + \nu)$ where ν is Poisson's ratio. C_{sd} appears as a fixed parameter because of the rigid boundary condition imposed parallel to the disc in the K–G loop calculation. For the present application, C_{sd}, is adjustable, according to Equation 23a, in order to allow for various transformation strains that might occur during precipitation. Writing this in terms of transformation strains [2] ε_{33}, $\varepsilon_{11} = \varepsilon_{22}$ gives

$$C_{sd} = \frac{(\varepsilon_{33} - \varepsilon_{11})}{(\varepsilon_{33} + 2\varepsilon_{11})}\,\frac{(C_{11} - C_{12})}{(C_{11} + 2C_{12})} \tag{23b}$$

If the volume change appearing in the strength term in Equation 18b is set equal to that for one undersized or oversized atom, i.e.

$$\Delta V = \pi X_d V_{SF} S r_0^3 = V_{SF} V_a \tag{24a}$$

one obtains the contribution from one point source within the disc. This term is directly related to the displacement of a surface about the defect, i.e.

$$\Delta V^{\infty} = \int_0^{\pi} \mu_r(\phi, r) 2\pi r^2 \sin\phi \, d\phi = \frac{\Delta V}{\gamma} \quad (24b)$$

with the previously defined Eshelby factor, γ, appearing as a correction between the volume change for an infinite medium, ΔV^{∞}, and one that is finite, ΔV.

Displacements must be projected along specified column directions and superimposed in calculating $2M$. Because the symmetry axis for the field does not normally coincide with the column direction, additional terms are required for the projected field. The various angles in stereographic projection are shown in Fig. 4a. To project the radial component of the field, one multiplies by

$$P_r = \cos x_r = \cos s \cos\phi + \sin s \sin\phi \cos\alpha \quad (25a)$$

while for the projection of the tangential components, ϕ differs by $\pi/2$ and one multiplies by

$$P_t = \cos x_t = \cos s \cos\left(\phi + \frac{\pi}{2}\right) + \sin s \sin\left(\phi + \frac{\pi}{2}\right)\cos\alpha$$
$$= -\cos s \sin\phi + \sin s \cos\phi \cos\alpha \quad (25b)$$

The normal to the disc is along the z-axis, and $\boldsymbol{C}$ is a vector along the column direction which is confined to the xz plane. $\boldsymbol{r}$ is a vector extending to a point in the matrix with an orientation specified by the spherical angles ϕ, α. Spatial interrelationships are best visualized as stereographic projections of unit vectors. The angles s, χ, and ϕ form a spherical triangle having sides that are large circles on the surface of a sphere. α is the angle between planes with sides s and ϕ.

Equations 18a and b and 25a and b can be combined to define the projected displacement from the tetragonal point source

$$PRA(r, \phi, \alpha; r_0, h) = A_r P_r + A_t P_t \quad (26)$$

where A_r and A_t are the radial and tangential components of the field strengths and the notation PR designates the operation of projecting both the radial, P_r, and tangential, P_t, components of $\boldsymbol{A}$ on to a column $[h\,k\,l]$. In this case, the field obeys a simple inverse square law, which allows Equation 15a to be used.

$2M$ involves only the matrix with the precipitate excluded. For these considerations, the radial distance, r_c, locates the interface between the precipitate and matrix. It is measured radially from the centre of the precipitate. In treating a circular disc, it is convenient to define an angle, ϕ_0, that locates the disc edge, such that

$$r_c = (h/2)/\cos\phi \qquad \text{for } 0 \leqslant \phi < \phi_0$$

and

$$r_c = r_0/\sin\phi \qquad \text{for } \phi_0 \leqslant \phi \leqslant \frac{\pi}{2} \quad (27)$$

The radial integration used to obtain Equation 15a has introduced the term $r_c(\phi)^{2n-3}$ which tends to unity for strong fields, because $n \to 3/2$. It becomes $r_c(\phi)$ for weak fields with $n \to 2$. The angular transition, ϕ_0, requires the following two integrals

$$M \Big/ \frac{X_c}{V_a} e \left(\frac{\Delta V}{4\pi\gamma} k_o\right)^n = \frac{2}{(h/2)^{2n-3}} \int_0^{\phi_o} \int_0^{2\pi} |P_r(s, \phi, \alpha) A_r(\phi)$$
$$+ P_t(s, \phi, \alpha) A_t(\phi)|^n \cos\phi^{2n-3} \sin\phi \, d\alpha \, d\phi$$
$$+ \frac{2}{r_0^{2n-3}} \int_{\phi_o}^{\pi/2} \int_0^{2\pi} |P_r(s, \phi, \alpha) A_r(\phi)$$
$$+ P_t(s, \phi, \alpha) A_t(\phi)|^n \sin\phi^{2n-2} \, d\alpha \, d\phi \quad (28)$$

Because n is not an integer over the range of interest, all integrals must be evaluated numerically.

2.2. Finite disc

The field discussed in the previous section is useful for large distances with $r > 10r_0$ or for precipitates of small radius. At the shorter distances with $r < 10r_0$, corrections are required to a single asymptotic point defect field. The finite disc size requires a summation over a uniform distribution of asymptotic point defect fields located in each disc. The summation is written in integral form and represented by a sum of point sources when evaluated numerically. This method of generating the field which describes core displacements about a disc is reduced to a non-uniform and weighted distribution of asymptotic point sources. The details are described elsewhere [4]. The number of sources is minimized according to a *GLQ* scheme. This field is designated by $\mu_d(r, \phi, h, r_0)$. A distribution of point sources introduces terms involving r that depart from the simple inverse square law assumed in deriving Equation 15a. Consequently, one must begin with a more general equation for $2M$, i.e. Equation 4b. This is less convenient to deal with because of the trigonometric form which requires additional numerical calculations.

The contribution of the projected displacement from each point source located at position ij is given by the sum

$$PR\mu_d(r, \phi, \alpha, r_0, h) = \frac{\pi h r_0^2}{4V_a} X_c \sum_{j=1}^{n_j} \sum_{i=1}^{n_i} (1 + Z_j) w_j w_i$$
$$PR\mu_{ij}\left(r, \phi, \alpha, \tfrac{1}{2} r_0 (1 + Z_j), \frac{\pi}{2}(1 + Z_i)\right) \quad (29)$$

with the symbol PR indicating the projections of both radial and tangential components as previously described. Angular positions within the plane of the disc are determined by Z_i, and radial positions by Z_j which range from ± 1. Weights w_i and roots z_i can be found in the literature on numerical methods, (e.g. [7]).

The number of points necessary in the Gauss–Legendre quadrature (n_j, n_i) depends on the radial distance from the disc [4]. For points very close to the disc, larger numbers such as $n_i = 30$, $n_j = 10$, are necessary, whereas for larger distances, smaller numbers (e.g. $n_i = 8$, $n_j = 6$) are sufficient. $2M$ can be written

as follows

$$2M = 2\,\frac{X_B - X_{mB}}{X_d V_p}\int_{r_c}^{\infty}\int_0^{2\pi}\int_0^{\pi} \times\left\{1-\cos\left[k_0\,\frac{(P_r A_r + P_t A_t}{r^2}\right]\right\} r^2 \sin\phi\,\mathrm{d}\phi\,\mathrm{d}\alpha\,\mathrm{d}r \tag{30}$$

Because the atom fraction, X_B, of undersize or oversize B atoms is fixed by the overall composition of the alloy, the number of sites occupied by disc centres per unit volume can be determined by

$$\frac{X_c}{V_a} = \frac{X_B - X_{mB}}{X_d V_p} \tag{31}$$

where X_{mB} is the fraction of B atoms remaining in the matrix, which is given by the metastable diagram, X_d is the reaction of B atoms in the precipitate, and $V_p = \pi h r_0^2$. h and r_0 are the height and radius of the disc. If X_d is known, V_p, the average volume per disc can be obtained from the data.

In order to compare with *XRD* data, five integrations are required, two for the source [4], and triple integration, over r, ϕ and α for $2M$. The computer time is reduced in a numerical calculation by taking a limited number of optimum locations and weighting factors for point defect sources within each disc according to Gauss–Legendre quadrature. This can be directly used for the angular integration (over ϕ, α). Radial integration goes to infinity and can be solved by a corresponding method [8]. However, the contributions of large distances, r, are small and can be neglected. Then it is possible to replace the upper limit with a finite value and apply also the Gauss–Legendre quadrature. Moreover, the integration space within the matrix is reduced by symmetry to the upper hemisphere of spherical angles. This can be further reduced for a single disc. The resulting formula for $2M$ calculation is

$$2M = \pi^2\left(\frac{X_B - X_{mB}}{X_d V_p}\right)\sum_{i=1}^{n_i}\sum_{j=1}^{n_j} W_i W_j \times\left\{\int_{\mu_c}^{\infty}\left\{1-\cos k_0\left[P_r A_r\left(\frac{\pi}{2}(1+Z_i),\,\pi(1+Z_j)\right)\Big/ r^2 + P_t A_t\left(\frac{\pi}{2}(1+Z_i),\,\pi(1+Z_j)\right)\Big/ r^2\right]\right\} r^2\,\mathrm{d}r\right\}\sin\frac{\pi}{2}(1+Z_i) \tag{32}$$

where the internal, radial, integration can be solved as described above with about 10–15 points.

2.3. Stair-step pairs of discs

A two-step source is described by taking disc centres that are spaced by a distance $2a$ at positions $\pm a\,c_x$, $\pm a\,c_y$, $\pm a\,c_z$ with c_x, c_y, c_z designating direction cosines for the line connecting disc centres [4]. The displacement field for a two-step pair of discs is formulated in terms of radial distance, r, from the centre of the line connecting disc centres. In general, rotational symmetry for unprojected displacements about the z-axis, is lost in the two-step source.

The projected displacements for the two-step pair is given by

$$PR\mu_p(r, \phi, \alpha; h, r_0, a, c_x, c_y; c_z) = PR[\mu_d(r_1, \phi_1, \alpha_1; h, r_0) + \mu_d(r_2, \phi_2, \alpha_2; h, r_0)] \tag{33}$$

with the locations of discs 1 and 2 given in terms of a common origin. Equation 33 represents the sum of displacements from all point sources located within both discs. For a [1 0 1] stair-step, $c_x = c_z = 1/2^{1/2}$, with $c_y = 0$. Other orientations of the type $\langle 1\,1\,0\rangle$ are possible and likely. In $2M$ calculations, the integral must be carried out numerically according to the procedure described by Equation 32 but by using projected displacements for the pair. The volume term V_p now refers to the volume of both discs. Both displacement terms in the argument blow up at each of the source centres and must be avoided. Strictly, the volume occupied by the two discs should also be excluded from the integration. For $r \geqslant 20r_0$, the integral can be carried out as if there is only one source of double strength located halfway between the pair of discs. Also, the quantity X_c represents the fraction of lattice sites coinciding with a two-step origin. This may be calculated from the atomic fraction of beryllium, $X_d = \frac{1}{2}$, the dimensions of the disc and the density of two-step precipitation. The density and mean distance between centres can be calculated by placing centres on an average cubic lattice.

In order to compare with XRD data, an additional triple integration is required for $2M$ factors over r, ϕ, and α. Again, the computer time for $2M$ calculations is reduced in a numerical calculation by taking a limited number of optimum locations and weighting factors for point defect sources within each disc. The integration space within the matrix needed to carry out Equation 32 is reduced by symmetry to the upper hemisphere of spherical angles. Calculation time is further reduced by interpolation from carefully selected initial points.

3. Experimental procedure

A polycrystalline commercial Brush 25 alloy with Cu–11.50 at % Be–0.23 at % Co was used throughout this study. An initial solution treatment of 3/32 in ($\sim$ 2.38 mm) thick discs was carried out in an argon atmosphere at 780 °C for 15 min. Quenching was into a brine solution, and surfaces were subsequently acid cleaned and electropolished. Between ageing treatments, samples were stored at -4 °C.

Two sets of XRD data were collected. For the first, the MoK_α doublet was used to give the higher order (4 2 2) and (3 3 3, 5 1 1) peaks in addition to the (1 1 1). (2 0 0), (2 2 0), (3 1 1), (2 2 2) and (4 0 0). This gives somewhat larger k_0 values for the measurement of weaker displacement fields that are expected for the shorter ageing times, i.e. the period from 16–256 min at 200 °C. Fig. 6 shows a hardness increase extending to one-third of the maximum value after 256 min. Fig. 7 illustrates two pairs of first- and second-order peaks from (1 1 1) and (2 0 0) planes. In each case, the broad

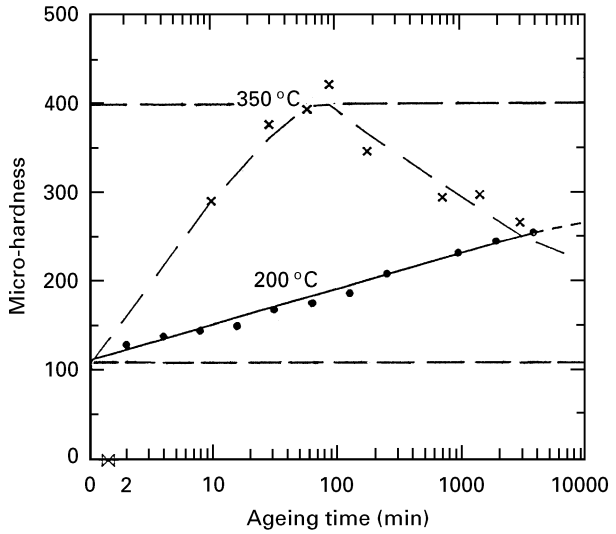

Figure 6 Micro-hardness of Cu–Be alloy aged at 200 and 350 °C for different times.

low-angle portion of the intensity distribution is largely due to quasiline. Going from first- to second-order doubles the value of k_0. The effect of an increase in this parameter is readily seen in the (2 0 0) and (4 0 0) data. An examination of the data after a 256 min ageing treatment, illustrates the discontinuous nature of the quasiline intensity. The (1 1 1), (2 2 2) pair show much smaller quasiline intensity than the (2 0 0), (4 0 0) pair. This choice of crystal directions represents an extreme for demonstrating this effect in the present alloy. An isotropic displacement field would give a quasiline that increases smoothly with k_0 (or 2θ) irregardless of $(h\,k\,l)$. This is seen from Equation 16a which depends upon k_0 but not the crystal direction. An explanation of this behaviour seems to require a displacement field that is anisotropic, and as will be seen later, preferred orientations of the precipitate with respect to the free surface play an equally important role.

A second and more accurate set of data was obtained using monochromatic Cu$K_{\alpha 1}$ radiation. This was used for 16 and 64 h at 200 °C. The matrix scattering effects are large enough so that the highest orders obtained with MoK_α are not needed. A position-sensitive detector, fine-focus copper X-ray tube, and an incident $K_{\alpha 1}$ monochromator, gave a high density of data points with high statistical accuracy. These data points are shown in Fig. 8a and b for (1 1 1), (2 0 0), (2 2 0), (3 1 1), (2 2 2), and (4 0 0) peaks. If this is related to hardness, an ageing time of 64 h at 200 °C, resulted in an increase which is halfway to its maximum value. An examination of the (4 0 0) peak, in Fig. 8b shows that it has become largely quasiline.

Table I gives a listing of $2M$ values obtained from Pearson VII non-linear fitting [9] of the intensity distributions shown in Fig. 8a and b. Equations 1–3 were used to partition integrated intensities for the Bragg peak, static diffuse, and quasiline peaks. Theory also predicts that the widths of these distributions increases in the order given. If more than one fit is obtained with a similar misfit, or R factor, the width criterion typically limits the fit to one $2M$ value. A modified non-linear Levenberg–Marquardt method was used to search for a best fit. When the convergence was very slow, an interactive routine with graphics was more efficient in terms of computer time. Individual curves are shown for the three components in Fig. 8a and b. The fitted curves using three symmetrical functions are generally good, although small oscillations are apparent between the best fit using three symmetrical functions and the data. Some additional error is also expected in all determinations due to the use of symmetrical functions for fitting scattering with a degree of asymmetry. Despite these concerns, the results lead to consistent findings when fitted to one of the models already discussed.

4. Fitting of data models

In order to arrive at models that relate to our data, the anisotropic behaviour of $2M$ and quasiline shifts were examined. These findings are listed in Tables II and

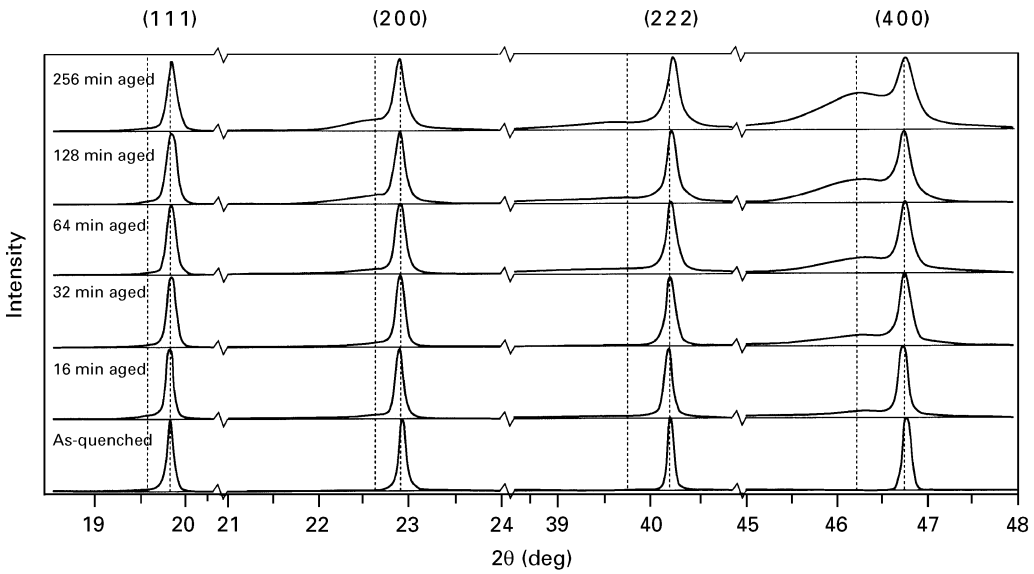

Figure 7 Mo$K_{\alpha 1}$ diffraction peaks for (1 1 1), (2 0 0), (2 2 2), and (4 0 0) from a Cu–11.50 at % Be–0.23 at % Co alloy aged for designated times at 200 °C.

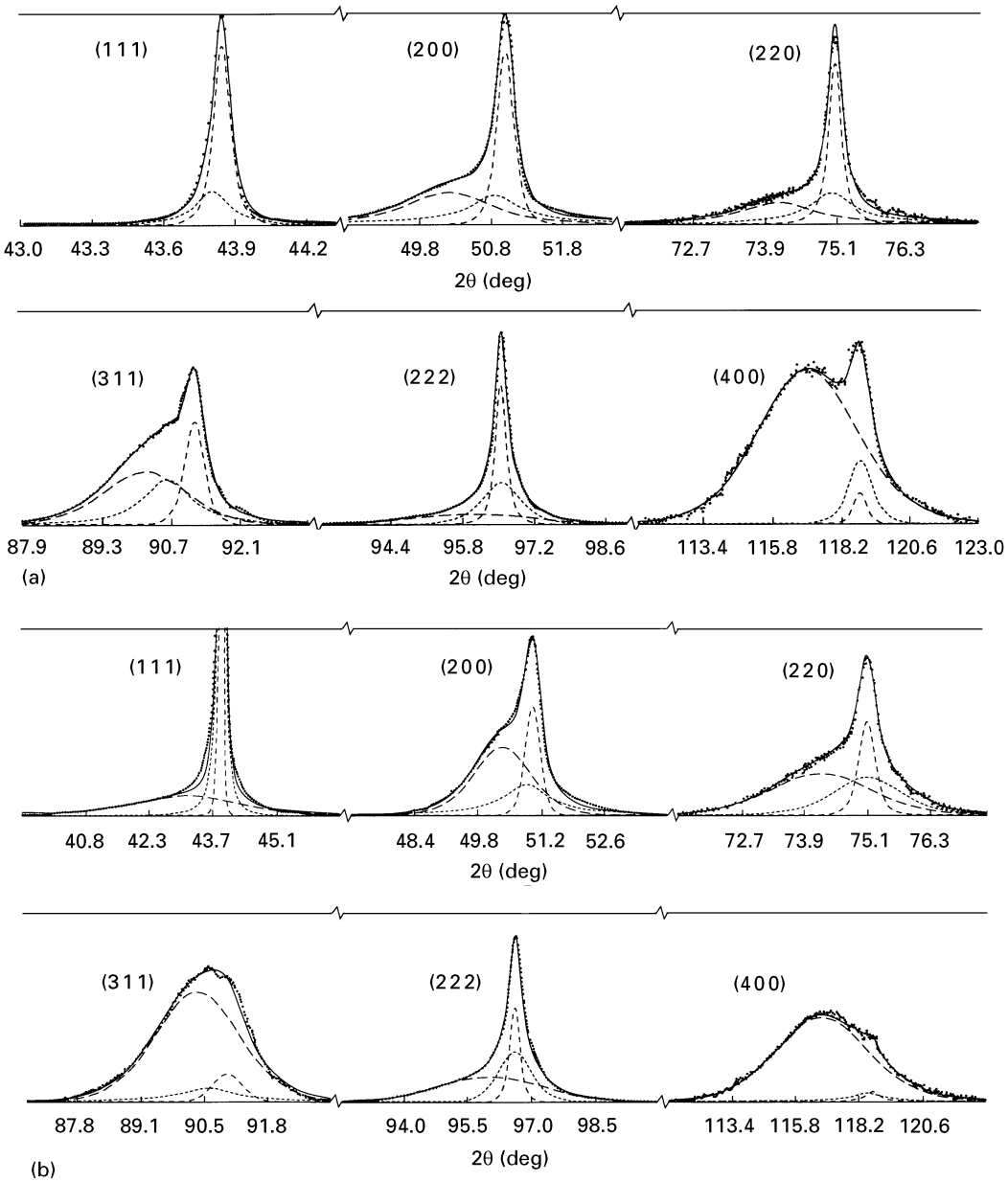

Figure 8 Monochromatic Cu$K_{\alpha 1}$ diffraction peaks with position sensitive detector: (a) aged 16 h at 200 °C, (b) aged 64 h at 200 °C.

TABLE I Experimental 2M values from Pearson VII fits of 16 and 64 h data at 200 °C with R values. Fitting was constrained to satisfy Equations 1–3, with quasiline, static diffuse, and Bragg decreasing in width

(hkl)	$2M_{16}$	$2M_{64}$	R_{16} (%)	R_{64} (%)
(1 1 1)	0.14	0.12	5.9	5.3
(2 0 0)	0.30	0.27	3.8	3.7
(2 2 0)	0.28	0.35	5.3	3.5
(3 1 1)	0.42	0.63	2.8	4.9
(2 2 2)	0.27	0.35	3.6	3.0
(4 0 0)	1.00	1.00	3.7	4.1
Scale	3.79	4.77		

III for disc diameters of 50–90 nm. Because of the high density of precipitates found in the present alloy, disc separations were taken to be small and range roughly from one to one-half of the disc diameter. Parameters common to all calculations include an atomic fraction of $X_B = 0.113$ for beryllium in the alloy and a precipitate composition of $X_d = 0.5$ [10]. At 200 °C, the metastable diagram extrapolates to $X_{mb} = 0.06$ [10] and transformation strains of $\varepsilon_{11} = \varepsilon_{22} = 0.114$, $\varepsilon_{33} = -0.338$ were used for the 16 h treatment while $\varepsilon_{11} = \varepsilon_{22} = 0.125$, $\varepsilon_{33} = -0.360$ have been reported after 64 h [2]. Both combinations established the tetragonality parameter, C_{sd}, by Equation 23b.

The 2M factor is most sensitive to the disc dimensions as seen in the scale factors listed in Table II. With large displacements and the altered changes in disc shapes associated with changes in thickness and radius, linear relationships cannot be expected from Equation 32. Scale factors show a less than linear increase with disc volume. In order to assess relative changes as they relate to anisotropy, all entries are normalized relative to the largest values which occur at the (4 0 0). Although small systematic differences in the normalized entries are found between the various

TABLE II $2M$ trends calculated with various dimensions for a single disc and different separation distances for [1 1 0] pairs. Scale factors and normalization for the (4 0 0) at 0° are listed.

hkl	S_j^0	$2M$ for $2r_0$ (nm), h (nm), $2a$ (nm)					
		6.0, 0.29, –	9.0, 0.29	6.0, 0.29, 3.0	6.0, 0.29, 7.0	6.0, 0.58	6.0, 0.58, 3.0
1 1 1	54.7	0.078	0.076	0.089	0.083	0.095	0.109
	54.7	–	–	0.078	0.070	–	0.096
2 0 0	0	0.266	0.266	0.282	0.272	0.308	0.324
	90	0.020	0.023	0.022	0.020	0.025	0.029
	90	–	–	0.023	0.019	–	0.029
2 2 0	45	0.285	0.282	0.320	0.307	0.333	0.368
	45	–	–	0.278	0.260	–	0.332
	45	–	–	0.288	0.275	–	0.331
	45	–	–	0.288	0.275	–	0.331
	90	0.043	0.043	0.046	0.042	0.053	0.058
	90	–	–	0.043	0.038	–	0.058
3 1 1	25.2	0.590	0.586	0.620	0.613	0.643	0.663
	25.2	–	–	0.582	0.559	–	0.638
	72.4	0.121	0.119	0.133	0.121	0.145	0.167
	72.4	–	–	0.119	0.105	–	0.150
	72.4	–	–	0.128	0.099	–	0.138
	72.4	–	–	0.130	0.126	–	0.139
2 2 2	54.7	0.309	0.315	0.340	0.332	0.358	0.395
	54.7	–	–	0.295	0.282	–	0.357
4 0 0	0	1.000	1.000	1.000	1.000	1.000	1.000
	90	0.086	0.086	0.086	0.080	0.103	0.114
	90	–	–	0.086	0.083	–	0.107
Scale factors		5.12	7.88	6.94	6.26	8.00	10.32

TABLE III Calculated $2M$ values for four models to be compared with data from samples aged for 16 and 64 hrs at 200 °C

		$2M$ for $2r_0$ (nm), h (nm), $2a$ (nm)			
(hkl)	S_j^0	16 h		64 h	
		5.0, 0.29, –	3.6, 0.29, 2.0	6.4, 0.29, –	4.8, 0.29, 3.0
1 1 1	54.7	0.079	0.083	0.081	0.087
	54.7	–	0.077	–	0.076
2 0 0	0	0.269	0.262	0.270	0.274
	90	0.022	0.020	0.025	0.024
	90	–	0.021	–	0.024
2 2 0	45	0.290	0.320	0.294	0.318
	45	–	0.283	–	0.297
	45	–	0.277	–	0.275
	45	–	0.277	–	0.275
	90	0.042	0.042	0.046	0.032
	90	–	0.069	–	0.047
3 1 1	25.2	0.593	0.589	0.592	0.618
	25.2	–	0.588	–	0.589
	72.4	0.119	0.124	0.125	0.133
	72.4	–	0.118	–	0.121
	72.4	–	0.133	–	0.101
	72.4	–	0.110	–	0.110
2 2 2	54.7	0.308	0.320	0.316	0.341
	54.7	–	0.294	–	0.299
4 0 0	0	1.000	1.000	1.000	1.000
	90	0.082	0.084	0.092	0.093
	90	–	0.082	–	0.095
Scale factors		4.28	4.08	6.08	5.92

models, in most cases these would not be experimentally observable. The most obvious anisotropy is seen to be given by $2M_{90}$ (2 0 0) $< 2M$ (1 1 1) $< 2M_0$ (2 0 0), with a similar relation for the (4 0 0), (2 2 2) combination. One finds a factor of 10 in $2M$ between the extreme orientations of $\{2\,0\,0\}$ and $\{4\,0\,0\}$ combinations, i.e. with $\phi = 0$, and 90°. This is due to the large anisotropy associated with the tetragonal transformation strain and the elastic anisotropy of the copper-rich matrix.

Results similar to Table II cannot be fitted to experimental values if all $\{1\,0\,0\}$ orientations of $\{1\,0\,0\}$ disc planes relative to the free surface are equiprobable. The data strongly suggest that (0 0 1) disc planes in surface grains prefer to be parallel to the free surface. The following normalized weighting factor was used for disc planes [11].

$$\omega_j = p_j \exp(-C_2 \sin^2 S_j) \Big/ \sum_j^m p_j \exp(-C_2 \sin^2 S_j) \tag{34}$$

with p_i designating the number of equivalent disc planes at an angle S_j with respect to the diffracting planes (hkl) which are parallel to the free surface, and C_2 determines the degree of preferred orientation. That is, $C_2 = 0$ corresponds to the random or equiprobable case. With $C_2 > 0$ a degree of preferred orientation is introduced. It should be noted that data were collected using symmetrical Bragg–Bretano diffraction optics and grains having (1 1 1), (2 0 0), (2 2 0),

TABLE IV Normalized, orientation corrected $2M$ values for four models showing agreement with data from 16 and 64 h samples aged at 200 °C. Data from Table III are used

hkl	$2M$ for $2r_0$ (nm), h (nm), $2a$ (nm)					
	Exp., 16 h	5.0, 0.29, –	3.6, 0.29, 2.0	Exp., 64 h	6.4, 0.29	4.8, 0.29, 3.0
1 1 1	0.14	0.093	0.095	0.12	0.098	0.098
2 0 0	0.30	0.269	0.275	0.27	0.270	0.273
2 2 0	0.28	0.300	0.304	0.35	0.311	0.303
3 1 1	0.42	0.549	0.557	0.63	0.549	0.558
2 2 2	0.27	0.360	0.365	0.33	0.380	0.381
4 0 0	1.00	1.000	1.000	1.00	1.000	1.000
Scale factor	3.79	3.61	3.59	4.77	4.92	4.91
C_1, C_2		1.02, 2.39	0.98, 2.40		1.00, 2.15	1.01, 2.23

and (3 1 1) planes parallel to the surface were examined at each of the Bragg–like reflections. The angles S_j in Tables II, III and V (see later) are located in Fig. 4a in terms of the precipitate planes $[h'\,k'\,l']$ $(=\langle 1\,0\,0\rangle)$ and the previously mentioned diffraction planes.

It is convenient to introduce a second parameter, C_1, into the orientation fitting procedure which provides a test of scaling for the various models. Both C_1 and C_2 are fitted using data given in Table III for single and paired discs as indicated by the following relation

$$C_1(2M) = \sum_j^m \omega_j(2M_j) \tag{35}$$

where $2M$ is relatable to the experimentally determined $2M$ of Table I, and $2M_j$ are the corresponding theoretical predictions from one of the models of a fixed orientation.

Results from the $2M$ fitting procedure are given in Table IV for samples aged at 200 °C for 16 and 64 h. Both C_1 and C_2 determinations are remarkably consistent at (1.02, 2.4) and (1.00, 2.15). With C_1 very close to unity, the $2M$ scaling from all models is very good. C_2 is of considerable interest for several reasons. Direct precipitate intensity data from the (0 0 1), (1 0 0) demonstrates that the (0 0 1) habit planes prefer to be parallel to the surface [2]. The probability for this orientation, obtained from relative integrated intensites, is found to be 2.25 relative to the random case with all three orientations having a 1/3 probability. Calculations using experimental C_2 values, give ratios of 2.54 and 2.44, for samples aged 16 and 64 h, respectively. Although the present values correspond to a 200 °C ageing treatment and data obtained from direct scattering correspond to a sample aged at 315 °C, the small differences are likely to be experimental error. These values of C_2 are used later for determining quasiline shifts.

Differences found in $2M$ (Table IV) for single discs and pairs of discs cannot be distinguished experimentally. However, one finds that disc diameters are localized to the range from 3.6–5.0 nm after ageing for 16 h and 4.8–5.4 nm after 64 h. In each case, a height of 0.29 nm is taken and the temperature is 200 °C. The displacement fields for each of these models are shown in Figs 9–11. Experimental and calculated values of $2M$ are plotted in Fig. 12.

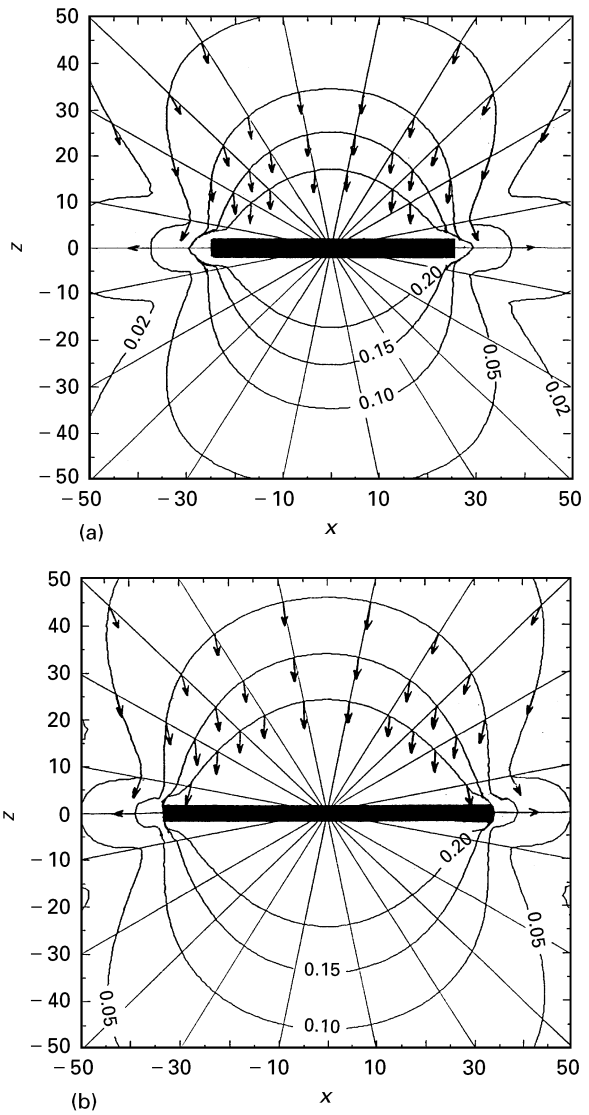

Figure 9 Displacement magnitude contours in Å about a Cu–50 at % Be disc with a 0.29 nm thickness and a radius of (a) 5.0 nm, (b) 6.4 nm.

To distinguish further between the various models, particularly between single discs and pairs, quasiline shifts were examined. This presents added difficulties in that a volume of severe deformation must be

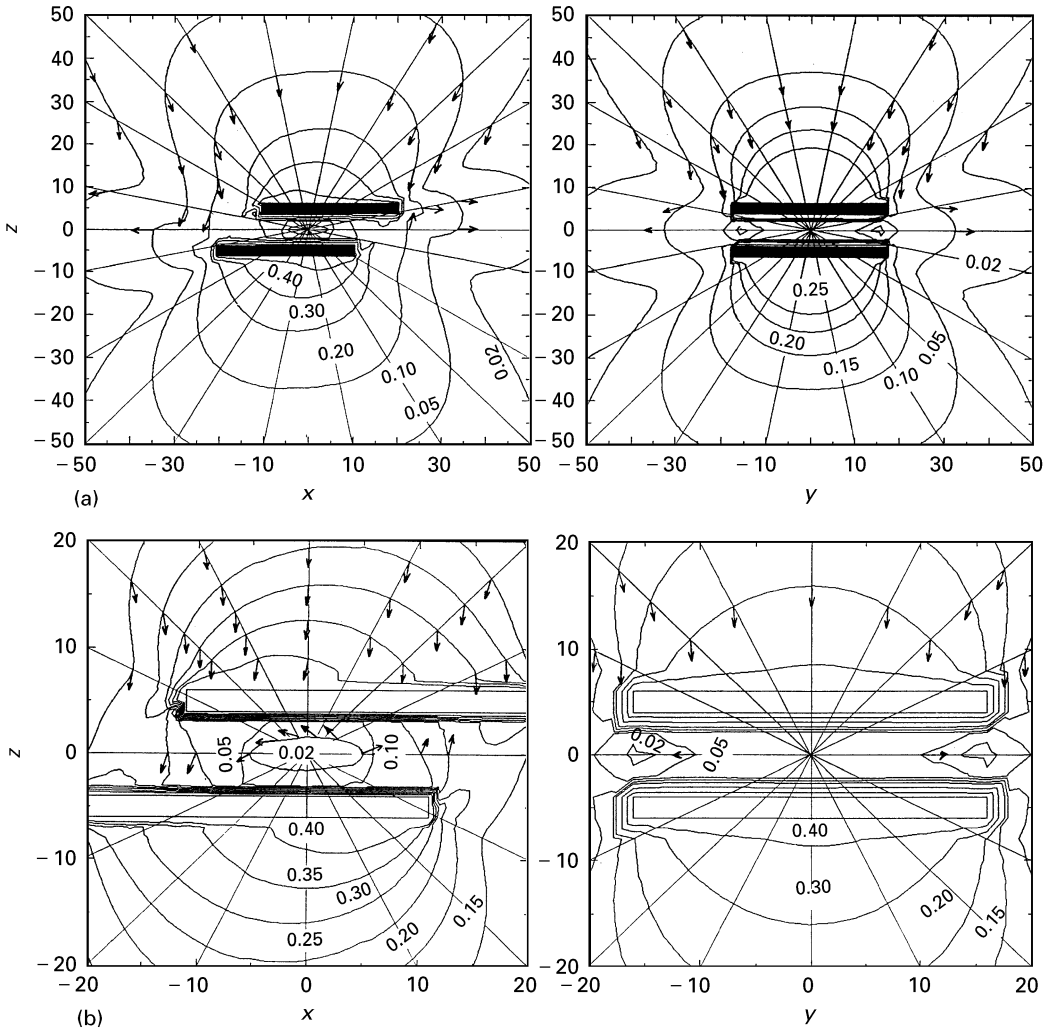

Figure 10 Displacement magnitude contours in Å about a stair-step pair of discs at 45° (16 h model). (a) $2r_0 = 3.6$ nm, $2a = 2.0$ nm, and 0.29 nm thick. Side and front views with selected displacement directions shown by arrows. (b) Same as (a) but the centre zone expanded.

defined as limiting contours in Figs 9–11. An examination of the schematic representation of Fourier coefficients shown schematically in Fig. 3b defines n_Q as the maximum number of cells along columns $(h\,k\,l)$ that correspond to a severely distorted zone about a precipitate. For the lowest order matrix peak, this is roughly equal to the diameter of a disc for pairs and the radius for single discs both measured from the centre. An examination of Figs 9–11 indicates that a displacement magnitude of 0.15 in Å would represent a reasonable first estimate for the bounding displacement surface of the severely distorted zone. It represents a displacement about twice the mean thermal displacement in copper at room temperature. The size of the zone is related to the scaling of diffraction phenomena. It is not constant but increases as the square root of distance to the $(h\,k\,l)$ point in reciprocal space (see Equations 8c and 17). At the larger distances in crystal space, the inverse square displacement law may be used to estimate changes in the bounding surface which defines the highly distorted zone associated with each quasiline. This results in surfaces of reduced displacements or larger volumes in crystal space for the highly distorted zones as one goes to $(h\,k\,l)$ points at larger distances in reciprocal space. The following relation was used to locate the displacement surfaces

$$\mu_s(h\,k\,l) = 0.15\,\frac{k_0(1\,1\,1)}{k_0(h\,k\,l)} \tag{36}$$

Increasing the volume for averaging relative column displacements results in smaller changes in the interplanar spacing at the higher orders of like planes. Table III shows this decrease at the (4 0 0) with (2 0 0) giving maximum values. Here normalization is at the (2 0 0). Equation 24 in King [4] is used for calculating the primary quasiline shifts.

Table V contains primary spacing changes from four models which could not be distinguished from an analysis of $2M$. The larger differences between single discs and stair-step pairs is encouraging. Before relating Table V to experimental shifts through weighting factors, the experimental conditions are re-examined as they are related to the weighting factors. To unscramble the three types of scattering, Pearson VII functions were fitted to profile data with a single Pearson VII used to describe the integrated intensity and peak position for a quasiline at each $(h\,k\,l)$ location. This is justified by the dominance of the largest $2M$ in locating the observed intensity distribution. That is, columns H_{hkl} making the smallest angle, S,

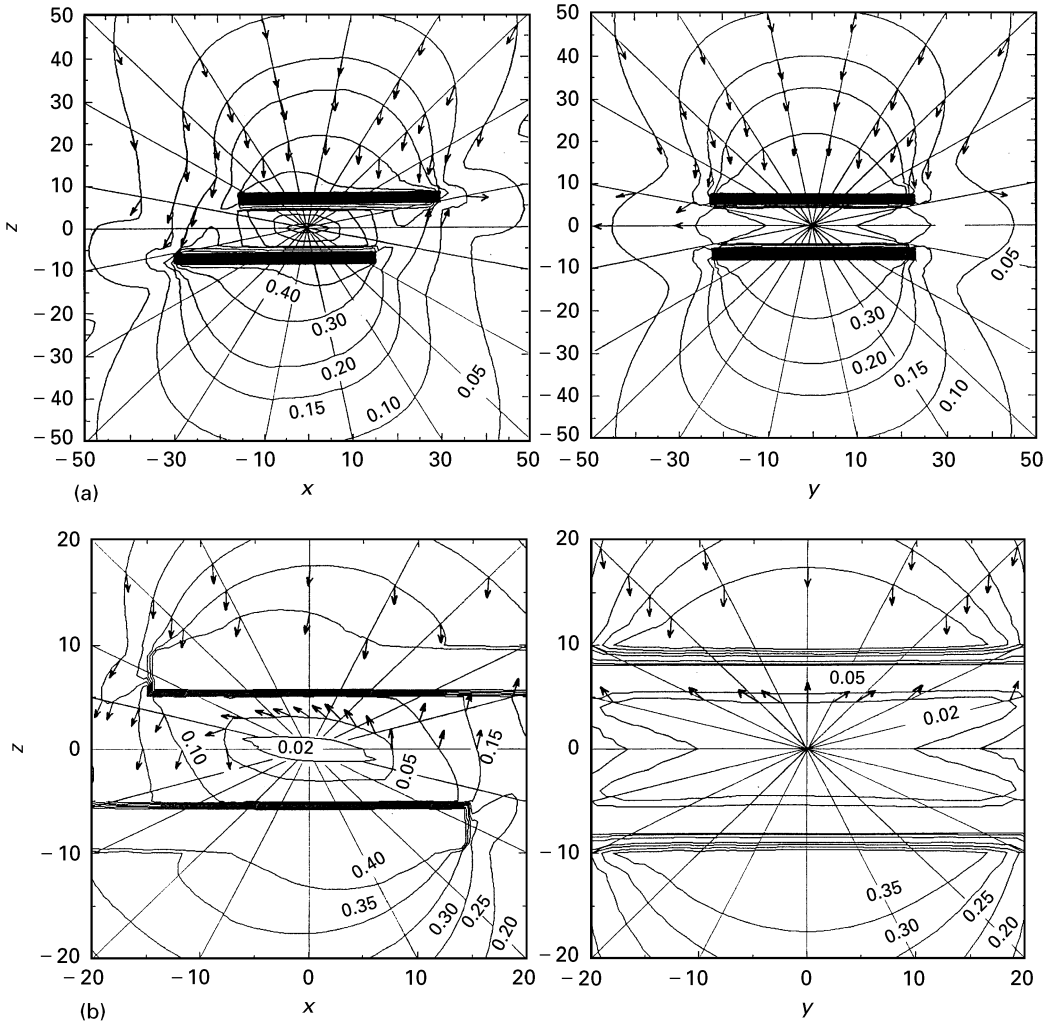

Figure 11 Displacement magnitude contours in Å about a stair-step pair of discs at 45° (64 h model). (a) $2r_0 = 4.8$ nm, $2a = 3.0$ nm, and 0.29 nm thick. Side and front views with selected displacement directions shown by arrows. (b) Same as (a) but the centre zone expanded.

with the disc normal, [0 0 1] are the dominant contributors to quasilines due to their large values of $2M$ and their strong orientation preference for disc alignment with the surface. The experimental shifts are compared with a first moment analysis using the results from each model. This requires relative quasiline intensity weighting as well as orientation factors. The procedure and findings are described in detail in the next section. Two of the four models become preferred after examining the weighted quasiline shifts.

5. Discussion

Precipitation in a commercial polycrystalline Cu–11.55 at % Be–0.23 at % Co alloy was examined after ageing at 200 °C for 16 and 64 h using relative integrated intensities and peak shifts. This ageing treatment was found to give about one-half the maximum hardness increase. Data were analysed by using simplified models to describe the atomic displacement field around disc-shaped precipitates in an elastically anisotropic medium. Bragg-like XRD profiles were partitioned into three components, i.e. Bragg, static diffuse, and quasiline for each $(h\,k\,l)$ distribution. The fitting procedure made use of symmetrical Pearson VII functions which were constrained by theoretical considerations involving the relative integrated intensities and widths of the three components.

With the present polycrystalline samples and Cu$K_{\alpha 1}$ X-radiation, the depth of penetration is limited to the average grain size which permits only grains at the surface to be examined. This presents a modified environment relative to interior grains that are completely surrounded by solid material. The possibility of surface relaxation in a system such as CuBe exhibiting zones of severe deformation must be considered in explaining the large anisotropies in the quasiline intensity and peak shift data. Displacement anisotropy as seen in $2M$ and related changes in the average lattice parameter become enhanced because disc-shaped precipitates tend to align parallel to the free surface. If one considers diffraction from (0 0 2) oriented grains, the corresponding (0 0 1) habit planes of disc-shaped precipitates tend to align preferentially parallel to the free surface. This is preferred by a factor of ~ 2.5 relative to a completely random arrangement of (1 0 0) orientations. Likewise, for grains having (1 1 3) matrix planes parallel to the surface, the nearest (0 0 1) precipitate planes are inclined by 25.2° which are preferred over those at 72.4°. These preferences, as described by the orientation function, Equation 34, located the major Bain strain in precipitates and

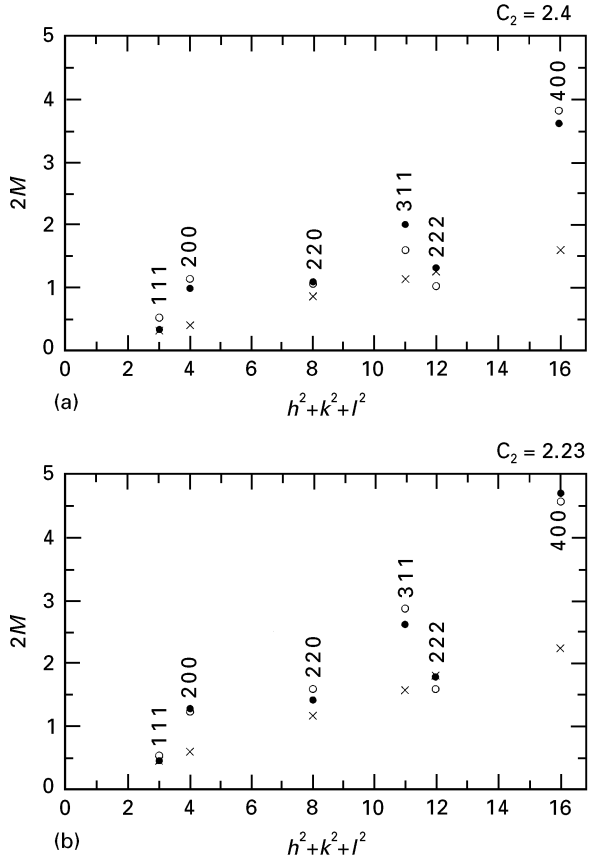

Figure 12 (●) Experimental and (○, ×) calculated values of $2M$ for samples aged for (a) 16 and (b) 64 h at 200 °C. The h, k, l indices of the six measured peaks are indicated. The theoretical values were calculated by using the disc-pair model (Table IV) and assuming both the random distribution of precipitates (×), with all {1 0 0} orientations of {1 0 0} disc planes equiprobable relative to the free surface, and (○) the preferred orientation of the defects parallel to the free surface.

TABLE V Estimates of primary quasiline shifts, Δd_{pj}, for two discs and [1 1 0] pairs used for comparing with samples aged for 16 and 64 h at 200 °C. Volumes based upon a 0.015 nm displacement surface were averaged. Scale factors in 0.0001 nm and normalization for (2 0 0) at 0° are listed

hkl	S_j^0	Δd_{pj} for $2r_0$ (nm), h (nm) $2a$ (nm)			
		5.0, 0.29, –	3.6, 0.29, 2.0	6.4, 0.29, –	4.8, 0.29, 3.0
1 1 1	54.7	0.426	0.360	0.653	0.376
	54.7	–	0.258	–	0.35
2 0 0		1.000	1.00	1.000	1.000
	90	− 0.022	− 0.12	0.018	0.006
	90	–	− 0.14	–	− 0.014
2 2 0	45	0.294	0.358	0.298	0.359
	45	–	0.277	–	0.268
	45	–	0.220	–	0.227
	45	–	0.220	–	0.227
	90	− 0.205	− 0.104	− 0.123	− 0.136
	90	–	− 0.073	–	0.098
3 1 1	25.2	0.576	0.486	0.611	0.606
	25.2	–	0.353	–	0.240
	72.4	− 0.118	0.023	− 0.141	0.055
	72.4	–	0.040	–	0.060
	72.4		− 0.054	–	− 0.086
	72.4	–	− 0.014	–	0.024
2 2 2	54.7	0.221	0.119	0.260	0.171
	54.7	–	0.071	–	0.091
4 0 0	0	0.72	0.471	0.55	0.359
	90	− 0.148	− 0.090	− 0.180	− 0.094
	90	–	0.008	–	0.035
Scale factor		7.79	16.1	7.38	11.7

related matrix displacements so that the largest projections are along columns perpendicular to the free surface. The ability to attain this condition is limited by crystallographic relations between the matrix grains and the (0 0 1) habit plane of the precipitates.

A similar argument holds for changes in the average lattice parameters within the severely distorted zone as determined from the experimental positions of the quasiline peaks. The tendency for the largest changes in lattice parameter to be perpendicular to the surface can be tested without an elastic displacement model. Tetragonal elastic Bain-like strains appear in the matrix in response to thin coherent disc-shaped precipitates having been subjected to large tetragonal Bain strains. The various spacing changes are interrelated through an average cell which is obtained by deforming the cubic cell of the matrix. For small changes in the cubic cell, the spacing changes become

$$\Delta d_t = [(h^2 + k^2)\Delta a + l^2 \Delta c]/(h^2 + k^2 + l^2)^{3/2} \quad (37)$$

The change, Δa, is along the cubic axes [1 0 0] and [0 1 0] parallel to the disc, while Δc is perpendicular along [0 0 1] columns. These are representative of the average tetragonal cell within the highly distorted zone and introduce phase shifts which provide an estimate of the various quasiline peak positions. The measured spacing changes from quasilines are determined by averaging over crystallographically inter-related orientations and a quasiline weighting factor, q_j

$$\langle \Delta d \rangle = \sum_j \omega_j \, q_j \, \Delta d_j \quad (38a)$$

with

$$q_j = \frac{Q(M_j)}{\sum_j Q(M_j)}. \quad (38b)$$

ω_j has already been defined by Equation 34, with $C_1 = 1$ and C_2 determined by $2M$ calculations, $Q(M_j)$ is defined by Equation 3, and Δd_j by Equation 37. Intensity weighting of Δd_j is carried out using the $2M$ values listed in Table III in the exponential form of Equation 3. Individual peaks normally treated equally in the multiplicity of cubic reflections become unequal in intensity and are shifted. These weighted components play a key role in the first moment intensity analysis of the data. However, the overall trends are still maintained if a linear weighting scheme is used instead of the exponential relation given by Equation 3. A weighted least squares analysis yields $\Delta c =$ 0.0040 nm, $\Delta a = 0.0005$ nm for 16 h and 0.0042 nm, 0.0008 nm for 64 h.

The previous calculation demonstrates that an average tetragonal cell with the major change, Δc,

TABLE VI Normalized orientation and intensity weighted estimates of quasiline shifts (in 0.0001 nm) for a tetragonal cell: two single discs and [1 1 0] pairs are compared with data from 16 and 64 h samples aged at 200 °C. Data from Table V are used

$2r_0$ (nm)	h (nm)	$2a$ (nm)	Quasiline shifts								
			hkl								
			111	200	220	311	222	400	Scale factor	Tetr. %	$\Delta c, \Delta a$
–	16 h	exp	0.39	1.00	(0.54)	0.37	0.17	0.36	23	–	–
–	–	Tetr	0.48	1.00	0.40	0.48	0.24	0.49	19.9	100	40.0, 5.0
5.0	0.29	–	0.50	1.00	0.38	0.50	0.25	0.56	22.2	65	29, 6
3.6	0.29	20	0.44	1.00	0.34	0.420	0.17	0.47	24.1	33	16, 6
–	64 h	exp	0.54	1.00	0.31	0.31	0.17	0.41	22	–	–
–	–	Tetr	0.56	1.00	0.44	0.49	0.28	0.50	20.8	100	42, 8
6.4	0.29	–	0.67	1.00	0.42	0.49	0.31	0.43	20.7	65	27, 10
4.8	0.29	3.0	0.50	1.00	0.38	0.37	0.23	0.41	22.5	48	22, 8

perferentially directed towards the free surface, provides a good quantitative estimate of the observed quasiline peak positions (see Table VI) when appropriate weighting factors are introduced. The fractional changes of the cubic cell are all positive with the sum giving a small positive increase in the cell volume relative to the cubic cell of the as-quenched alloy. This can be related to composition shifts of -5.2% and -6.1% Be for 16 and 64 h using Vegards Law, i.e. by dividing the fractional volume change by the volume size factor ($=-0.2645$). This gives very good agreement with a low-temperature extrapolation of the previously published metastable diagram [10].

Thus far, the $2M$ analysis has not been able to determine whether single discs or stair-step pairs of discs best fit our data. Lattice parameter changes have been calculated from each of these models; however, neither model includes the effect of discs that surround the primary model. Secondary discs are arranged in unknown arrangements and must be included with the primary models to describe the full deformation in the severely deformed zone. The fractional volume change resulting from discs subjected to a Bain distortion is negative, which introduces a positive volume change in the highly distorted zone. In view of the preceding calculation, it will be assumed that this expanded zone averages to a tetragonal cell. Primary cells are always in close proximity to a highly deformed zone, whereas the secondary field is produced by discs acting over a range of distances and locations making it more uniform. The new lattice of the highly distorted zone includes a sum of both contributions, i.e.

$$\Delta d_j = \Delta d_{pj} + \Delta d_{sj} \tag{39}$$

where Δd_{pj} is obtained from the primary model and Δd_{sj} remains as an unknown d-spacing change from secondary discs, as given by Equation 39. Primary spacing changes for single discs are based upon tetragonal symmetry. Although pairs appear to give orthorhombic displacements, the departure from tetragonal symmetry is small and neglected.

The optimum secondary parameters, Δc_s and Δa_s, are obtained by varying Δd_{sj} in a weighted least squares fit of the data using equations 38a, b and 39. Table VI shows the resulting fit from this procedure. Stair-step pairs best fit the normalized pattern of experimental shifts for both ageing times. Normalized values are typically within 25%, which represents an expected overall error in our procedure. However, the experimental departure for the (2 2 0) in the 16 h data set appears to be anomalous with respect to all other points. The preceding exploratory calculation based upon a tetragonal unit cell and single primary disc calculations give similar results with normalized sets showing greater departures from the experimental data than the pair models. For the 16 h sample and a pair model, the secondary contribution is 33% while for 64 h it is 48%. Both are determined from relative scale factors. With disc calculations, the secondary contribution to the spacing change becomes dominant at 65%. When all of the spacing data are examined collectively, the stair-step pair with a secondary field becomes the preferred model for making quantitative estimates.

Spacing changes from (2 0 0) calculations in Table VI combined with secondary spacing changes give an average cell expansion along the c-axis of $+1.3\%$ within the highly distorted zone, while along the perpendicular directions it is only about $+1/9$ of this value. Our best Vegards Law estimate for the composition shifts, obtained from the pair model and the tetragonal cell, are 5.3 and 6.3 at % Be. This locates the metastable boundary at 6.0 (16 h) and 5.0 at % Be (64 h) for GP zones in a Cu–11.3 at % Be binary alloy. 0.2 at % Be was subtracted from the original 11.5 at % Be ternary alloy for beryllide formation making it comparable to the binary with 11 at % Be. Although a downward shift in this boundary is expected as the transformation progresses, a 1% shift in boundary composition cannot be stated with certainty because of possible errors in the data and the method of peak separation.

It is instructive to compare previous results obtained from a sample aged at 315 °C for 15 and 30 min with the present results for a sample aged at 200 °C for 16 and 64 h. Both samples were cut from the same alloy, had the same prior solution treatments, and both ageing treatments were close to the half maximum hardness. At the higher temperature, single flattened ellipsoids of revolution gave diameters

estimated at 9 and 20 nm and average thicknesses of one and two unit cells, respectively. At 200 °C, quantitative estimates of the diameters for stair-step pairs give 3.6 and 4.8 nm, a height of one unit cell (0.29 nm), and a pair spacing which appears to increase with time.

At this point, it is interesting to note several points of agreement with results obtained from diffuse X-ray scattering [12] which was carried out with a binary Cu–10.9 at % Be alloy at 265 °C for 100 and 200 min. It was reported that single and multilayered {1 0 0} Be-rich planes in a stair-step configuration are in agreement with the scattering data. Multi-layered stair-steps become preferred with increasing ageing time. Also, displacements go to zero after 5–7 layers or 0.9–1.3 nm which is in very good agreement with our results from a ternary alloy of similar Cu–Be composition but a somewhat lower annealing temperature. This, of course, represents half the spacing of the stair-step pairs obtained independently from a completely different method. Arrays having a large number of well-spaced parallel discs are not likely because of the absence of low-angle scattering peaks in the present samples [2].

Quasilines became dominant after ageing at 315 and 200 °C. At the higher temperature, quasiline shifts were much smaller and could be predicted from a system of randomly located single discs, within experimental error. A small quasiline shift is expected at 315 °C and is accounted for in the theory. Quasiline shifts are more obvious at 200 °C and are likely to result from both severe displacement fields from discs and a reduction of the berylluim content in the matrix. Both effects combine and cannot be reliably separated within the secondary parameters of the 200 °C data.

When (h 0 0) quasiline widths are intercompared at 200 °C versus 315 °C, the quasilines sharpen with increasing disc size. The disc size at the higher temperature is about 2–3 times larger and quasiline sharpness is scaled accordingly. Ageing at 200 °C gave quasilines that are obviously broader when compared at the half maximum hardness level.

Estimates of the relative densities of disc centres from Equation 31, using disc radii and the metastable boundary, give an order of magnitude higher density at 200 °C as compared with 315 °C. This high density of discs at the lower temperature would be supportive of a degree of local order about arrays of primary discs. The orientation data for discs and the secondary fields would be consistent with a mix of discs oriented mainly parallel to the primary array and to a lesser extent some local discs are likely to be perpendicular [13]. The field from secondary discs maintains a tetragonal deformation which is also found from primary pairs. Cubic symmetry would require equiprobable disc orientations along all three cubic axes. However, the best fitted values of $\Delta c/\Delta a$ tend to be ~ 2.7 which comes close to the orientation preference for discs parallel to the free surface.

6. Conclusion

To conclude, we re-examine some general trends in the diffraction profiles of Figs 7, 8a and b. These may be inter-related with $2M$ in Table I. Fig. 2 illustrates relative partitioning into the three components. The most obvious change in profile results from the displacement and integrated intensity of the quasiline relative to the sharper Bragg peak and static diffuse peaks. Extreme profile changes are seen by comparing (h 0 0) with (h h h). This is especially true for the (4 0 0) and (2 2 2) with $2M = 3.79$ and 1.02 after 16 h ageing at 200 °C. For 64 h the (4 0 0), (2 2 2) values increase to $2M = 4.77$ and 1.67. At each of these times, the quasiline dominates the (4 0 0) while for the (2 2 2) the intensity partitioning into three components is more equally distributed. The (4 0 0) and (2 2 2) have the highest $(\sin\theta/\lambda)^n$ weight factors in $2M$ which favour quasiline partitioning in the higher order peaks. For the shorter times (Fig. 7), some quasiline is observed in the (4 0 0) after only 16 min at 200 °C, and reshaping occurs continuously from 16 min to the longest ageing time of 64 h. Quantitatively estimated pair diameters for the shorter times are given in Table VII and range from 2.1–3.0 nm for 16–128 min. Single disc models range from 3.0–4.2 nm leading to about one-third the maximum hardness [15]. Longer ageing times up to 64 h give a pair diameter of 4.8 nm at about one-half the maximum hardness.

TABLE VII Diameter estimates for single, $2r_s$, and paired discs, $2r_p$, [15] for short times at 200 °C

$2r_s$ (nm)	3.0	3.2	3.6	3.9	4.2
$2r_p$ (nm)	2.1	2.3	2.6	2.8	3.0
t (min)	16	32	64	128	256

A re-examination of the displacement models of Figs 9–11 illustrates that the major displacements are located within the disc radius for single discs and a disc diameter for pairs. These are oriented perpendicular to the discs giving the maximum column projections along the [0 0 1] direction. At large distances, displacements become radial and small. A system of [0 0 1] columns oriented perpendicular to the discs are able to accumulate the largest displacements over the integration for $2M$. Columns of the type [0 0 4] are most favourable in every respect and tend to partition into quasilines for both single disc and pair models, whereas columns of the type [4 0 0] and [0 4 0] represent the opposite extreme for accumulated projected displacements and would tend to favour Bragg and SDS partitioning. Columns of the (2 2 2) type tend to have an intermediate to low accumulation of projected displacements because of its 54.7° inclination with the major displacement and disc cross-section. The symmetry change resulting from [1 0 1] pairs gives two values for $2M$; however, this is not large enough to be observable. The fortuitous combination of the largest accumulation of displacements and an orientation preference for [0 0 1] columns satisfies one condition for making age-hardenable Cu–Be alloys unique in demonstrating quasiline partitioning. This is contrasted with (h h h) reflections where such preferences do not exist.

Quasiline enhancements occur for the (1 1 3) component within the overall multiplicity. Large accumu-

lations of projected displacements are found along columns making a 25.2° angle with the disc normal. Columns oriented at 72.4° become influenced by reduced projections from large projection angles, a displacement limiting cusp, and a small disc cross-section. With an orientation enhancement for [1 1 3] columns, this becomes competitive with [0 0 l] type columns for a large 2M and quasiline formation.

Tetragonal quasiline shifts are determined by changes in d-spacings averaged over highly distorted zones. These local spacing changes are best related to the difference in projected displacements as one steps from cell to cell along oriented columns. One can express the local spacing change in terms of the projected displacement gradient times the height of the cells. Averaging over all columns gives an average gradient for oriented columns in the highly distorted zone. A comparative re-examination of the (2 0 0) or (4 0 0) quasiline shift data relative to the nearby (1 1 1) or (2 2 2) show large differences. The former give large shifts and the latter are much smaller. If one were to define the limiting surface at ~ 0.015 nm for the severely deformed zone, [0 0 l] columns of cells contains the highest average projected displacement gradient, whereas [h 0 0] type columns average to the smallest. This is true for both discs and pairs. If one examines [h h h] column projections, the average gradient is intermediate. They become smaller for [h h h] columns intersecting the highly disturbed zones of [1 0 1] stair step pairs. Table V illustrates these differences in average gradient for each direction. This reduction in quasiline shift, along with the reduced shift for the (1 1 3), become determining factors when deciding upon a single disc model or the preferred stair-step model which better approximates the displacement gradients.

Acknowledgements

Funding for this research was made available by National Science Foundation Grant no. DMR-8818013. We thank Dr Amitava Guha, Brush Wellman Inc., Cleveland, OH, for providing samples and his preliminary discussions that provided a very useful background for this research.

References

1. C. R. HOUSKA, *Acta Crystallogr.* **A49** (1993) p. 771.
2. C. H. WU, PhD thesis, Virginia Polytechnic Institute and State University (1993).
3. M. A. KRIVOGLAZ, "Difrakciya rentgenovskich luchey i neitronov v neidealnych kristalach" (Naukova Dumka, Kiev, 1983).
4. C. R. HOUSKA, R. KUŽEL, *J. Mater. Sci.*, submitted.
5. H. W. KING, *ibid.* **1** (1966) p. 79.
6. D. T. KEATING and A. N. GOLAND, *J. Appl. Phys.* **39** (1968) 6018.
7. B. CARNAHAN, H. A. LUTHER and J. O. WILKES, "Applied Numerical Methods" (Wiley, New York, 1969).
8. R. PIESSENS, E. de DONCKER-KAPENGA, C. W. UEBERHUBER and D. K. KAHANER, QUADPACK, (Springer, New York, 1983).
9. M. M. HALL, V. G. VEERARAGHAVEN, H. RUBEN and P. G. WINCHELL, *J. Appl. Crystallogr.* **10** (1977) 66.
10. D. J. CHAKRABARTI, D. E. LAUGHLIN and L. E. TANNER, *Bull. Alloy Phase Diag.* **8** (3) (1987) 269.
11. P. ČAPKOVÁ and V. VALVODA, *Czech. J. Phys.* **B24** (1974) 891.
12. Y. M. KOO and J. B. COHEN, *Acta Metall.* **37** (1989) 1295.
13. V. PEROVIC, G. R. PURDY, L. M. BROWN, *ibid.* **29** (1981) 889.
14. B. HE, PhD thesis, Virginia Polytechnic Institute and State University (1992).

Received 10 August 1995
and accepted 3 September 1996